ARMY RESEARCH LABORATORY

Navier-Stokes Predictions of Pitch-Damping for Axisymmetric Shell Using Steady Coning Motion

Paul Weinacht
Walter B. Sturek
Lewis B. Schiff

ARL-TR-575 September 1994

NOTICES

Destroy this report when it is no longer needed. DO NOT return it to the originator.

Additional copies of this report may be obtained from the National Technical Information Service, U.S. Department of Commerce, 5285 Port Royal Road, Springfield, VA 22161.

The findings of this report are not to be construed as an official Department of the Army position, unless so designated by other authorized documents.

The use of trade names or manufacturers' names in this report does not constitute indorsement of any commercial product.

REPORT DOCUMENTATION PAGE

Form Approved
OMB No. 0704-0188

1. AGENCY USE ONLY *(Leave blank)*	2. REPORT DATE	3. REPORT TYPE AND DATES COVERED
	September 1994	Final, January 1989 - June 1993

4. TITLE AND SUBTITLE

Navier-Stokes Predictions of Pitch-Damping for Axisymmetric Shell Using Steady Coning Motion

5. FUNDING NUMBERS

PR: 1L161102AH43

6. AUTHOR(S)

Paul Weinacht, Walter B. Sturek, and Lewis B. Schiff

7. PERFORMING ORGANIZATION NAME(S) AND ADDRESS(ES)

U.S. Army Research Laboratory
ATTN: AMSRL-WT-PB
Aberdeen Proving Ground, MD 21005-5066

8. PERFORMING ORGANIZATION REPORT NUMBER

9. SPONSORING/MONITORING AGENCY NAMES(S) AND ADDRESS(ES)

U.S. Army Research Laboratory
ATTN: AMSRL-OP-AP-L
Aberdeen Proving Ground, MD 21005-5066

10.SPONSORING/MONITORING AGENCY REPORT NUMBER

ARL-TR-575

11. SUPPLEMENTARY NOTES

12a. DISTRIBUTION/AVAILABILITY STATEMENT

Approved for public release; distribution is unlimited.

12b. DISTRIBUTION CODE

13. ABSTRACT *(Maximum 200 words)*

Previous theoretical investigations have proposed that the side force and moment acting on a body of revolution in steady coning motion could be related to the pitch-damping force and moment. In the current research effort, this approach is applied to produce predictions of the pitch-damping for axisymmetric shell. The flow fields about these projectiles undergoing steady coning motion are successfully computed using a parabolized Navier-Stokes computational approach which makes use of a rotating coordinate frame. The governing equations are modified to include the centrifugal and Coriolis force terms due to the rotating coordinate frame. From the computed flow field, the side moments due to coning motion, spinning motion, and combined spinning and coning motion are used to determine the pitch-damping coefficients. Computations are performed for two generic shell configurations: a secant-ogive-cylinder and a secant-ogive-cylinder-
boattail. Predictions are made for various length-to-diameter ratios and supersonic Mach numbers and comparisons made with results obtained using a previously published inviscid code. Results are also obtained for a series of ogive-cylinder configurations which have been tested in an aerodynamics range. The comparisons between computational predictions and the range data confirm the validity of the theoretical approach.

14. SUBJECT TERMS	15. NUMBER OF PAGES
Projectiles, Aerodynamic Characteristics, Computational Fluid Dynamics, Pitch-Damping	35
	16. PRICE CODE

17. SECURITY CLASSIFICATION OF REPORT	18. SECURITY CLASSIFICATION OF THIS PAGE	19. SECURITY CLASSIFICATION OF ABSTRACT	20. LIMITATION OF ABSTRACT
UNCLASSIFIED	UNCLASSIFIED	UNCLASSIFIED	UL

INTENTIONALLY LEFT BLANK.

Acknowledgment

The authors wish to acknowledge Mr. Bernard Guidos for his contributions in reviewing this report.

INTENTIONALLY LEFT BLANK.

Table of Contents

INTENTIONALLY LEFT BLANK.

List of Figures

INTENTIONALLY LEFT BLANK.

I. INTRODUCTION

Prediction of the in-flight motion of projectiles requires the determination of the aerodynamic forces and moments that act on the body. These aerodynamic forces and moments may be determined by experimental or theoretical means, such as Computational Fluid Dynamics. From a computational standpoint, much of the research effort has focused on determining the static aerodynamics such as drag and pitching moment. Only a limited number of studies have focused on numerical prediction of dynamic aerodynamic derivatives such as pitch-damping force and moment. In the current research effort, a parabolized Navier-Stokes technique has been adapted to predict the pitch-damping force and moment using steady coning motion.

By applying linear flight mechanics theory such as that developed by Murphy,[1] it can be shown that aerodynamic side force and moment coefficients acting on a projectile in steady coning motion can be related to the pitch-damping force and moment coefficients. In steady coning motion, the longitudinal axis of the missile performs a rotation at a constant angular velocity about a line parallel to the free-stream velocity vector and coincident with the projectile center of gravity (CG), while oriented at a constant angle with respect to the free-stream velocity vector. This is shown schematically in Figure 1. The use of steady coning motion to determine the pitch-damping aerodynamic coefficients provides an interesting and cost-effective approach for determining the aerodynamics that are normally associated with unsteady or time-dependent motions.

Previously, Tobak, Schiff, and Peterson[2] examined the aerodynamics of bodies of revolution in coning motion and proposed that the nonlinear aerodynamic forces and moments acting on a body performing large amplitude non-planar motions could be composed of four characteristic motions: (1) steady angle of attack, (2) pitching motion, (3) rolling motion, and (4) coning motion. Typically, the linear aerodynamic force and moment formulation considers only forces and moments due to the first three motions, and assumes that a non-planar motion can be described by the vector sum of two independent planar motions. The addition of coning motion allows for coupling between planar motions in the nonlinear formulation. Their nonlinear theory also confirms the linear theory result that the side force and moment due to coning motion is related to the linear pitch-damping coefficients.

To provide additional validation for the theory, Schiff and Tobak[3] performed wind tunnel experiments on a conical body undergoing separate or combined spinning and coning motions. Their results showed that at low angles of attack the slopes of the side force and moment with angle of attack normalized by the coning rate were in good agreement with predictions of the damping-in-pitch force and moment coefficients obtained using linearized theory. They also demonstrated that the Magnus force and moment (variation of side force and moment with spin rate and angle of attack) was small; thus, the linear pitch-damping coefficients could be determined from the side force and moment due to coning alone.

Subsequently, Schiff[4] computed the supersonic inviscid flow about a conical body undergoing coning motion. To compute the flow around the body in coning motion, Schiff made use of a rotating coordinate frame. Within the rotating coordinate frame, the flow was steady; thus, the steady Euler equations could be solved. The governing equations were modified to include the centrifugal and Coriolis force terms. His computed results com-

pared well with experimental results and with estimates of pitch-damping coefficients using a linear theory. Later studies by Agarwal and Rakich,[5] and Lin[6] also employed rotating coordinate frames to compute the supersonic viscous flow about conical bodies in coning motion. More recently, Weinacht and Sturek[7] performed computations for finned projectiles in coning motion to determine the pitch-damping coefficients.

In each of the previous efforts, the pitch-damping coefficients were determined from the side moment due to steady lunar coning motion which required the Magnus moment to be neglected. The predictions of the pitch-damping coefficients presented in this report were determined from the side moment due to a specific combination of spinning and coning motion which allows the side moment due to this motion to be directly related to the pitch-damping force and moment coefficients. These motions will be defined in more detail in the next section.

In the current report, predictions of pitch-damping for axisymmetric shell were made using combined spinning and coning motions. The flow field about these projectiles in steady coning motion has been successfully computed using the parabolized Navier-Stokes (PNS) computational approach of Schiff and Steger.[8] The computations are performed in a rotating coordinate frame similar to that employed originally by Schiff. Code modification required to implement the rotating coordinate frame, including the addition of the centrifugal and Coriolis source terms and changes to the shock fitting algorithm, are discussed. From the computed flow field, the side moments due to coning motion, spinning motion, and combined spinning and coning motion are used to determine the pitch-damping coefficient. Computations have been performed for two generic shell configurations, a secant-ogive-cylinder (SOC) and a secant-ogive-cylinder-boattail (SOCBT). The PNS predictions are made for various length-to-diameter ratios and supersonic Mach numbers, and compared with predictions made using an Euler code originally reported by Schiff. Results are also presented for a series of ogive-cylinder configurations that have been fired through an aerodynamics range located at the former Ballistic Research Laboratory.[1] Comparison between PNS results and range data are made.

II. THEORETICAL BACKGROUND

In this section, the moment expansion of a symmetric missile is first introduced. Two types of coning motion are described and related to the pitching motion of the missile body. Finally, the moments produced by both types of coning motion are related to the various moment components in the moment expansion. In particular, the pitch-damping moment is related to the side moment due to coning motion.

[1]The U.S. Army Ballistic Research Laboratory was deactivated on 30 September 1992 and subsequently became a part of the U.S. Army Research Laboratory (ARL) on 1 October 1992.

1. Moment Expansion.

It is common in aeroballistic applications to utilize a missile-fixed, non-rolling coordinate system to describe both the kinematics and the system of forces and moments that act on the projectile in flight.[1] The non-rolling coordinate system affords some simplifications, particularly in describing the kinematics. In this report, the primary reason for initially describing the aerodynamic moments using the non-rolling coordinate system is the fact that the description is well-established. The non-rolling coordinate frame is an orthogonal right-handed system $(\tilde{x}, \tilde{y}, \tilde{z})$ centered at the body CG. The $\tilde{x}$-axis is aligned along the projectile longitudinal axis with the positive direction oriented towards the projectile nose. The $\tilde{z}$-axis is "initially" oriented downward with the $\tilde{x} - \tilde{z}$ plane perpendicular to the ground. The angular motion of the non-rolling coordinate frame is such that, with respect to an inertial frame, the $\tilde{x}$-component of the coordinate frame's angular velocity is zero. Although the time-dependent orientation of the non-rolling frame may be hard to visualize, the non-rolling frame is essentially equivalent to the "fixed-plane" coordinate system for small amplitude motions. In the fixed-plane coordinate system, the $\tilde{x} - \tilde{z}$ plane remains perpendicular to the ground for all time. Further details on these coordinate frames can be found in Reference 1.

The moment expansion developed by Murphy[1] for a symmetric missile in the non-rolling coordinate frame is shown in Equation 1. The moment formulation uses complex variables to separate the moment components, $\tilde{C}_m$ and $\tilde{C}_n$, that are oriented along the $\tilde{y}$ and $\tilde{z}$ axes, respectively. The third moment component, the roll moment, can be handled separately and is not of consequence in this study.

$$\tilde{C}_m + i\tilde{C}_n = [(\frac{pl}{V})C_{n_{pa}} + C_{n_a} - iC_{m_a}]\tilde{\xi} - \frac{i}{\gamma}[C_{m_q} + \gamma C_{m_{\dot{\alpha}}}]\tilde{\xi}' \tag{1}$$

In the moment expansion, the pitching moment coefficient, C_{m_a}, and pitch-damping moment coefficient, $C_{m_q} + \gamma C_{m_{\dot{\alpha}}}$, produce moments that are proportional to the complex yaw, $\tilde{\xi}$, and yawing rate, $\tilde{\xi}'$, respectively. (In the analysis presented here, there is no need to distinguish between pitch and yaw and the terms may be interchanged. The usage follows that of Murphy.[1]) The Magnus moment coefficient, $C_{n_{pa}}$, accounts for a side moment due to flow asymmetries from a combination of spin and angle of attack.

Experimental procedures to determine both the pitching and Magnus moments are conceptually easy to devise because these moments depend on the angle of attack and not the angular rate. For instance, the pitching and Magnus moments can be determined from wind tunnel measurements of pitch-plane and side moments on a spinning flight body held at a fixed angle of attack. Since this is a steady motion for axisymmetric bodies, computational analogs based on steady flow techniques can be easily implemented. In contrast, the fact that the pitch-damping moment is produced by the angular rate seems to imply that a time-dependent motion is required to produce the moment. One obvious unsteady motion that might be considered is a planar constant amplitude pitching motion. Experiments and computational approaches can be devised to determine the pitch-damping moment from unsteady motions, but this may be an unnecessary complication. It is possible to devise motions that still produce an angular rate, but when viewed in the appropriate coordinate system, are steady motions. Coning motion represents one such motion.

2. Relation Between Coning and Pitching Motions.

As was discussed previously, in steady coning motion, the longitudinal axis of the missile performs a rotation at a constant angular velocity about a line parallel to the free-stream velocity vector and coincident with the projectile center of gravity, while oriented at a constant angle with respect to the free-stream velocity vector. This is shown schematically in Figure 1. In the context of this report, coning motion also requires the center of gravity to traverse a rectilinear path at constant velocity. With respect to the non-rolling coordinate frame, the vertical and horizontal components of the angle of attack, α and β, vary in a periodic fashion as the projectile rotates about the free-stream velocity vector, as shown in Figure 2. However, the total angle of attack, $\alpha_t \approx \sqrt{\alpha^2 + \beta^2}$ is constant.

Both of these components of the angle of attack, when plotted as a function of time, are sinusoidal, constant amplitude pitching motions that are out of phase with each other by one quarter of a cycle, as shown in Figure 3. By decomposing coning motion in this fashion, it can be observed that coning motion contains a specific linear combination of two orthogonal planar pitching motions. As will be shown later, this particular combination of planar pitching motions yields a non-zero angular rate which is a requirement for producing the pitch-damping moment.

The term "steady coning motion" describes the rotation of the longitudinal axis of the body about the free-stream velocity vector, but does not completely describe the motion of the body. In particular, the projectile may rotate (or spin) about its longitudinal axis. In this report, two particular forms of coning motion, *steady lunar coning motion* and *steady combined spinning and coning motion*, are utilized. The two motions differ in their treatment of the angular velocity about the longitudinal axis.

In steady lunar coning motion, the angular velocity of the projectile results purely from the rotation of the projectile about the free-stream velocity vector. This produces a component of angular velocity along the projectile axis, which by definition is the spin rate of the projectile in the non-rolling coordinate system. The relation between spin rate, p, and coning rate, $\dot{\phi}$, for the case of steady lunar coning motion is

$$p = \dot{\phi} \cos \alpha_t = \dot{\phi}\gamma \quad . \tag{2}$$

In steady combined spinning and coning motion, the angular velocity of the projectile consists of the vector sum of two angular velocity vectors. The first vector produces a rotation of the projectile's longitudinal axis about the free-stream velocity vector (coning motion), $\vec{\dot{\phi}}$, and the second produces a rotation of the projectile about its longitudinal axis (spinning motion), $\vec{p}_{cf}$. In general, there is no requirement for the spin rate to be coupled to the coning rate. However, in the context of this report, combined spinning and coning motion requires that $\vec{p}_{cf}$ be equal in magnitude but opposite in sign to the component of $\vec{\dot{\phi}}$ along the longitudinal axis, $p_{cf} = -\dot{\phi}\, cos\alpha_t$. In this case, the total angular velocity of the body about the longitudinal axis is zero; hence, the spin rate in the non-rolling coordinate system is zero.

$$p = 0. \tag{3}$$

By specifying both the coning rate and the spin rate, the projectile angular motion is now completely defined. For the particular case of steady lunar coning, the motion can be decomposed into a combination of two orthogonal planar pitching motions, plus a spinning motion at angle of attack. Likewise, steady combined spinning and coning motion can be decomposed into two orthogonal pitching motions.

Planar pitching motion is clearly a time-dependent motion that produces a time-dependent flow field about the projectile. Steady lunar coning motion, on the other hand, should produce a steady flow field when viewed from the appropriate coordinate frame, such as the coning coordinate frame. In the coning frame, the x-axis is aligned with the longitudinal axis of the missile and is identical to the $\tilde{x}$-axis in the non-rolling frame. The plane formed by the x-axis and z-axis in the coning frame is parallel to the pitch plane. The y-axis is oriented normal to the pitch plane so that an orthogonal right-handed coordinate system is formed.

For steady lunar coning motion, the coning frame and the body rotate at the same angular velocity, thus there is no rotation of the pitch plane with respect to the body. Because the boundary conditions in the coning frame do not introduce any time-dependency into the problem, when observed from the coning reference frame, the resulting flow field is expected to be steady for small angles of attack and for small coning rates. It is important to realize that because the coning frame is rotating at a constant angular velocity and because the body does not rotate with respect to the coning frame of reference, there is no requirement for the body to have any special forms of geometric symmetry (i.e., axisymmetry) for steady flow to exist. Steady flow modeling techniques can be applied to determine the flow field due to steady lunar coning motion under the constraints that both the coning rate and the angle of attack are small. (Clearly, the flow may become unsteady at high coning rates or high angles of attack, in much the same way the flow over a body at fixed angle of attack at high incidence can become unsteady due to vortex shedding.)

For the case of steady combined spinning and coning motion, the body will rotate in the coning reference frame with a rate of rotation which is proportional to the coning rate, ($p_{cf} = -\phi \cos\alpha_t$). This rotation does not produce a time-dependent boundary condition for axisymmetric bodies and a steady flow field can exist. However, for non-axisymmetric bodies, the rotation of the body in the coning reference frame will produce a time-dependent (periodic) boundary condition and flow field. Thus, when combined spinning and coning motion is utilized, a steady flow field is only possible for axisymmetric bodies.

The steady nature of the flow in the coning frame makes the coning frame a desirable coordinate system for performing the fluid dynamic computations. Since the coning reference frame is a non-inertial system due to the rotation of the coordinate system, the governing equations for the fluid dynamics must be modified. Further details on the implementation of the rotating frame are provided in the discussion of the computational approach.

3. Relation Between Side Moment Due to Coning and Pitch-Damping Moment

To develop the relation between the side moment due to coning motion and the pitch-damping moment coefficient, it is convenient to resolve the moment components in non-

rolling coordinates into moment components in the coning coordinate frame. This relation is shown below. Here C_m is the in-plane moment coefficient (the moment which causes rotation of the body in the plane of the attack of attack), and C_n is the side moment coefficient (the moment that causes rotations of the body out of the angle of attack plane). Also shown are relations for the complex angle of attack and angular rate. These relations, valid for steady coning motion, have been simplified from the general case of arbitrary motion.[9]

$$\begin{aligned} C_m + iC_n &= ie^{-i\gamma\dot{\phi}t}(\tilde{C}_m + i\tilde{C}_n) \\ \tilde{\xi} &= \delta e^{i\gamma\dot{\phi}t} \\ \tilde{\xi}' \equiv \frac{d\tilde{\xi}}{d(\frac{s}{l})} &= i\delta\gamma\frac{\dot{\phi}l}{V}e^{i\gamma\dot{\phi}t} \end{aligned} \tag{4}$$

The moment formulation cast in terms of the in-plane and side moments can be written as follows:

$$C_m + iC_n = C_{m_\alpha}\delta + i\{(\frac{pl}{V})C_{n_{p\alpha}}\delta + \delta(\frac{\dot{\phi}l}{V})[C_{m_q} + \gamma C_{m_{\dot{\alpha}}}]\} \quad . \tag{5}$$

The resulting expression for the in-plane and side moments is independent of time for the case of steady coning and spinning motions. The in-plane moment (real part) results only from the pitching moment, while the total side moment (complex part) consists of contributions from the Magnus moment and pitch-damping moment. For each type of coning motion of interest in this report, the side moment assumes a particular form depending on the spin rate.

4. Side Moment for Lunar Coning Motion

As discussed previously, with respect to the non-rolling coordinate system, lunar coning motion produces a component of angular velocity along the longitudinal axis of the missile which by definition is the spin rate of the projectile (Equation 2). For this type of coning motion, the side moment can be written as

$$C_n = \delta(\frac{\dot{\phi}l}{V})(\gamma C_{n_{p\alpha}} + [C_{m_q} + \gamma C_{m_{\dot{\alpha}}}]) \quad . \tag{6}$$

The notation can be simplified by noting that the right-hand side of Equation 6 is simply the variation of side moment with coning rate, valid for linear variations of side moment with coning rate.

$$C_{n_{\dot{\phi}}} \equiv \frac{\partial C_n}{\partial(\frac{\dot{\phi}l}{V})} = \delta(\gamma C_{n_{p\alpha}} + [C_{m_q} + \gamma C_{m_{\dot{\alpha}}}]) \tag{7}$$

This relation is identical to that presented by Schiff and Tobak[3] for bodies of revolution. Equation 7 relates the variation of the side moment with coning rate, $C_{n_{\dot{\phi}}}$, to the pitch-damping coefficient, $[C_{m_q}+\gamma C_{m_{\dot{\alpha}}}]$, and the Magnus moment coefficient, $C_{n_{p\alpha}}$. Assuming that the side moment due to coning and the Magnus moment can be determined, this relation will allow the pitch-damping coefficient to be determined.

Despite the fact that lunar coning motion requires that the Magnus moment be determined (or assumed negligible) in order to determine the pitch-damping coefficient, this

motion is useful. Because the body does not rotate with respect to the pitch plane while undergoing coning motion, the flow, when observed in the coning coordinate frame, will be steady for axisymmetric and non-axisymmetric bodies. In many cases, particularly in supersonic flow, the Magnus moment may be neglected without any appreciable loss of accuracy. This approach has been recently applied to predict the pitch-damping for six-finned projectiles.[7] It should be noted that non-axisymmetric bodies with aerodynamic coefficients which exhibit a significant dependence on roll angle may need to be treated with a more general aerodynamic formulation[10, 11] than is presented here.

5. Side Moment for Combined Spinning and Coning Motion

The second type of coning motion discussed here uses a specific combination of coning and spinning motions to cause the component of the total angular velocity along the longitudinal axis of the missile to be zero. In other words, both the non-rolling coordinate frame and a body fixed coordinate frame will not rotate with respect to each other. Thus, the spin rate of the projectile, as observed from the non-rolling coordinates, is zero (Equation 3).

It should be noted, however, that the coning coordinate frame rotates with respect to the non-rolling coordinate frame and the body-fixed coordinate frame. In the coning coordinate frame, then, the body appears to perform a spinning motion since the body-fixed coordinate system rotates with respect to the coning coordinate frame. The spin rate in the coning coordinate frame will be $p_{cf} = -\gamma\dot{\phi}$. In this report, this motion is called "combined spinning and coning motion," because in the coning frame (which is the coordinate frame in which the computations are performed), the motion is a specific combination of spinning and coning motion. In the coning frame, this motion is a steady motion for axisymmetric bodies only. The presence of spin and angle of attack produces a periodic motion for non-axisymmetric bodies, thereby eliminating steady flow computational approaches from consideration.

For this type of coning motion, the side moment can be written as

$$C_n = \delta(\frac{\dot{\phi}l}{V})[C_{m_q} + \gamma C_{m_{\dot{\alpha}}}] \quad . \tag{8}$$

In this case, the side moment is directly proportional to the pitch-damping moment coefficient. In contrast to side moment due to lunar coning motion (Equation 6), no Magnus moment term appears here. Despite the simplicity of this expression, the Magnus effect has not been entirely removed from the problem. In the coning frame, the combination of angle of attack from the coning motion and the spinning motion produce a Magnus-like effect. Thus, any approach, whether it be computational or experimental, which uses this motion must be capable of modeling both of these effects. For example, a coarse grid CFD computation which does not resolve the viscous effects sufficiently to properly model the Magnus problem will produce pitch-damping results which will be in error by the degree to which the Magnus moment is improperly determined.

6. Side Force due to Coning Motions

Similar expressions relating side force due to coning to the pitch-damping force coefficient can be developed using the same approach used in analyzing the moments. The resulting expressions for the side force coefficients are similar in form to the expressions for the corresponding side moment coefficients for both types of motions.

For the case of lunar coning motion, the slope of the side force with coning rate, $C_{Y_{\dot{\phi}}}$, is a function of the pitch-damping force coefficient, $C_{N_q} + \gamma C_{N_{\dot{\alpha}}}$ and the Magnus force coefficient, $C_{Y_{p\alpha}}$.

$$C_{Y_{\dot{\phi}}} = \delta(\gamma C_{Y_{p\alpha}} + [C_{N_q} + \gamma C_{N_{\dot{\alpha}}}]) \tag{9}$$

Like the side moment due to lunar coning motion, determining the pitch-damping force coefficient from the side force due to lunar coning requires that the Magnus term be ignored or determined from another source.

For combined spinning and coning motion, the slope of the side force with coning rate, $C_{Y_{\dot{\phi}}}$, can be directly related to the pitch-damping force coefficient, $C_{N_q} + \gamma C_{N_{\dot{\alpha}}}$.

$$C_{Y_{\dot{\phi}}} = \delta[C_{N_q} + \gamma C_{N_{\dot{\alpha}}}] \tag{10}$$

7. Determination of the Pitch-Damping Coefficients.

The particular approach discussed here for determining the pitch-damping coefficients requires that the side force and moment due to coning ($C_{Y_{\dot{\phi}}}$ and $C_{n_{\dot{\phi}}}$) be determined. By computing the side force and moment at least two different coning rates, the variation of side force and moment can be determined. If steady combined spinning and coning motion is used, the pitch-damping coefficients are easily determined because these coefficients are directly proportional to the side force and moment due to coning as shown in Equations 8 and 10. On the other hand, if steady lunar coning motion is used, the Magnus force and moment must be determined from another source before the pitch-damping coefficients can be determined (Equations 7 and 9). Often the Magnus force and moment are small in relation to the pitch-damping coefficients and can be ignored when determining the pitch-damping coefficients from the side force and moment due to steady lunar coning motion.

Since many projectile and missile applications deal with small amplitude motions, it is customary to linearize the equations of motion. Thus, the pitch-damping force and moment coefficients often appear as $C_{N_q} + C_{N_{\dot{\alpha}}}$ and $C_{m_q} + C_{m_{\dot{\alpha}}}$ because the cosine of the angle of attack, γ, is nearly 1. This notation is adopted in the remainder of this report.

Finally, since the results presented in this report were obtained using steady motions, the two types of coning motion are referred to as "lunar coning motion" and "combined spinning and coning motion" in later sections of this report with the understanding that these are, in fact, steady motions.

III. COMPUTATIONAL APPROACH

Computation of the viscous flow field about the axisymmetric shell configurations was accomplished by solving the thin-layer Navier-Stokes equations using a PNS technique. The computations were performed in a coordinate frame that rotates at the coning rate of the projectile. The fluid flow relative to the rotating coordinate frame does not vary with time, allowing the steady (non-time-varying) Navier-Stokes equations to be applied. The solution of the steady Navier-Stokes equations can be performed at a reasonable computational cost. To implement the rolling coordinate frame, the governing equations were modified to include the effects of centrifugal and Coriolis forces. The steady, thin-layer Navier-Stokes equations in cylindrical coordinate form are

$$\frac{\partial \hat{E}}{\partial \xi} + \frac{\partial \hat{F}}{\partial \eta} + \frac{\partial \hat{G}}{\partial \zeta} + \hat{H}_c + \hat{H} = \frac{1}{Re}\left(\frac{\partial \hat{S}}{\partial \zeta} + \hat{S}_c\right) \quad . \tag{11}$$

Here, $\hat{E}$, $\hat{F}$, and $\hat{G}$ are the inviscid flux vectors, $\hat{S}$ is the viscous flux vector, $\hat{H}_c$ and $\hat{S}_c$ are inviscid and viscous source terms due to the cylindrical coordinate formulation, and $\hat{H}$ is the source term containing the Coriolis and centrifugal force terms which result from the rotating coordinate frame. Each of these vectors are functions of the dependent variables represented by the vector $q^T = (\rho, \rho u, \rho v, \rho w, e)$, where ρ and e are the density and the total energy per unit volume, and u, v, and w are the velocity components in the axial (x), circumferential (ϕ), and radial (r) directions. The flux terms are

$$\hat{E} = \frac{1}{J}\begin{bmatrix} \rho U \\ \rho u U + \xi_x \mathrm{p} \\ \rho v U \\ \rho w U \\ (e+\mathrm{p})U \end{bmatrix} \quad \hat{F} = \frac{1}{J}\begin{bmatrix} \rho V \\ \rho u V + \eta_x \mathrm{p} \\ \rho v V + \eta_\phi \mathrm{p}/r \\ \rho w V + \eta_r \mathrm{p} \\ (e+\mathrm{p})V \end{bmatrix} \quad \hat{G} = \frac{1}{J}\begin{bmatrix} \rho W \\ \rho u W + \zeta_x \mathrm{p} \\ \rho v W + \zeta_\phi \mathrm{p}/r \\ \rho w W + \zeta_r \mathrm{p} \\ (e+\mathrm{p})W \end{bmatrix}$$

$$\hat{H}_c = \frac{1}{Jr}\begin{bmatrix} \rho w \\ \rho u w \\ 2\rho v w \\ \rho(w^2 - v^2) \\ (e+\mathrm{p})w \end{bmatrix} \quad \hat{S} = \frac{1}{J}\begin{bmatrix} 0 \\ m_1 \dfrac{\partial u}{\partial \zeta} + m_2 \zeta_x \\ m_1 \dfrac{\partial v}{\partial \zeta} + m_2 \zeta_\phi / r \\ m_1 \dfrac{\partial w}{\partial \zeta} + m_2 \zeta_r \\ m_3 \end{bmatrix} \quad \hat{H} = \frac{1}{J}\begin{bmatrix} 0 \\ H_2 \\ H_3 \\ H_4 \\ H_5 \end{bmatrix} \tag{12}$$

$$\hat{S}_c = \frac{1}{J}\begin{bmatrix}
0 \\
-\zeta_x\frac{\partial}{\partial\zeta}\left((\mu+\mu_t)\frac{2w}{3r}\right)+\frac{\mu+\mu_t}{r}\left(\zeta_r\frac{\partial u}{\partial\zeta}+\zeta_x\frac{\partial w}{\partial\zeta}\right) \\
-\zeta_r\frac{\partial}{\partial\zeta}\left((\mu+\mu_t)\frac{v}{r}\right)+\frac{\zeta_\phi}{r}\frac{\partial}{\partial\zeta}\left((\mu+\mu_t)\frac{4w}{3r}\right) \\
\quad+\frac{2(\mu+\mu_t)}{r}\left(\frac{\zeta_\phi}{r}\frac{\partial w}{\partial\zeta}+\zeta_r\frac{\partial v}{\partial\zeta}-\frac{v}{r}\right) \\
-\frac{\zeta_\phi}{r}\frac{\partial}{\partial\zeta}\left((\mu+\mu_t)\frac{v}{r}\right)-\zeta_r\frac{\partial}{\partial\zeta}\left((\mu+\mu_t)\frac{2w}{3r}\right) \\
\quad+\frac{2(\mu+\mu_t)}{r}\left(\frac{-\zeta_\phi}{r}\frac{\partial v}{\partial\zeta}+\zeta_r\frac{\partial w}{\partial\zeta}-\frac{w}{r}\right) \\
-\zeta_x\frac{\partial}{\partial\zeta}\left((\mu+\mu_t)\frac{2uw}{3r}\right)+\frac{\zeta_\phi}{r}\frac{\partial}{\partial\zeta}\left((\mu+\mu_t)\frac{vw}{3r}\right) \\
\quad-\frac{\zeta_r}{r}\frac{\partial}{\partial\zeta}\left((\mu+\mu_t)\left(v^2+\frac{2}{3}w^2\right)\right)+\frac{(\mu+\mu_t)\,\zeta_r}{2r}\frac{\partial}{\partial\zeta}\left(q^2\right) \\
\quad-\frac{2w(\mu+\mu_t)}{3r}\left(\zeta_x\frac{\partial u}{\partial\zeta}+\frac{\zeta_\phi}{r}\frac{\partial v}{\partial\zeta}+\zeta_r\frac{\partial w}{\partial\zeta}\right) \\
\quad+\frac{(\mu+\mu_t)}{r}\left(u\zeta_x\frac{\partial w}{\partial\zeta}+\frac{v\zeta_\phi}{r}\frac{\partial w}{\partial\zeta}+w\zeta_r\frac{\partial w}{\partial\zeta}\right) \\
\quad+\frac{1}{\gamma-1}\left(\frac{\mu}{Pr}+\frac{\mu_t}{Pr_t}\right)\zeta_r\frac{\partial}{\partial\zeta}\left(a^2\right)
\end{bmatrix} \tag{13}$$

where

$$\begin{aligned}
H_2 &= r\rho\Omega_c^2\sin\alpha_t\cos\alpha_t\cos\phi-(x-x_{cg})\rho\Omega_c^2\sin^2\alpha_t+2\Omega_c\sin\alpha_t\cos\phi\rho v-2\Omega_c\sin\alpha_t\sin\phi\rho w \\
H_3 &= (x-x_{cg})\rho\Omega_c^2\sin\alpha_t\cos\alpha_t\sin\phi+r\rho\Omega_c^2\sin^2\alpha_t\cos\phi\sin\phi+2\Omega_c\cos\alpha_t\rho w \\
&\quad -2\Omega_c\sin\alpha_t\cos\phi\rho u \\
H_4 &= -r\rho\Omega_c^2\sin^2\alpha_t\sin\phi-r\rho\Omega_c^2\cos^2\alpha_t+(x-x_{cg})\rho\Omega_c^2\sin\alpha_t\cos\alpha_t\cos\phi \\
&\quad +2\Omega_c\sin\alpha_t\sin\phi\rho u-2\Omega_c\cos\alpha_t\rho v \\
H_5 &= (-(x-x_{cg})\Omega_c^2\sin^2\alpha_t\cos^2\alpha_t+r\Omega_c^2\sin\alpha_t\cos\alpha_t\cos\phi)\rho u \\
&\quad +((x-x_{cg})\Omega_c^2\cos\alpha_t\sin\alpha_t\sin\phi+r\Omega_c^2\sin^2\alpha_t\cos\phi\sin\phi)\rho v \\
&\quad +((x-x_{cg})\Omega_c^2\sin\alpha_t\cos\alpha_t\cos\phi-r\Omega_c^2\sin^2\alpha_t\sin^2\phi-r\Omega_c^2\cos^2\alpha_t)\rho w
\end{aligned} \tag{14}$$

$$\begin{aligned}
U &= u\xi_x \\
V &= u\eta_x+v\eta_\phi/r+w\eta_r \\
W &= u\zeta_x+v\zeta_\phi/r+w\zeta_r
\end{aligned} \tag{15}$$

$$m_1 = (\mu+\mu_t)(\zeta_x^2+(\zeta_\phi/r)^2+\zeta_r^2)$$

$$
\begin{aligned}
m_2 &= \frac{1}{3}(\mu+\mu_t)(\zeta_x\frac{\partial u}{\partial\zeta}+\frac{1}{r}\zeta_\phi\frac{\partial v}{\partial\zeta}+\zeta_r\frac{\partial w}{\partial\zeta}) \\
m_3 &= \frac{1}{(\gamma-1)}(\frac{\mu}{Pr}+\frac{\mu_t}{Pr_t})(\zeta_x^2+(\zeta_\phi/r)^2+\zeta_r^2)\frac{\partial a^2}{\partial\zeta}+\frac{1}{2}m_1\frac{\partial \mathrm{q}^2}{\partial\zeta} \\
&\quad +m_2(u\zeta_x+\frac{v}{r}\zeta_\phi+w\zeta_r) \qquad (16)\\
a^2 &= \frac{\gamma \mathrm{p}}{\rho} \qquad (17)\\
\mathrm{q}^2 &= u^2+v^2+w^2 \qquad (18)
\end{aligned}
$$

$$
\begin{array}{lll}
\xi_x = 1/x_\xi & & \\
\eta_x = J(r_\xi\phi_\zeta-\phi_\xi r_\zeta) & \eta_\phi = J(x_\xi r_\zeta) & \eta_r = J(-x_\xi\phi_\zeta) \\
\zeta_x = J(\phi_\xi r_\eta - r_\xi\phi_\eta) & \zeta_\phi = J(-x_\xi r_\eta) & \zeta_r = J(x_\zeta\phi_\eta) \\
J = 1/\left(x_\xi\left(\phi_\eta r_\zeta-\phi_\zeta r_\eta\right)\right) & &
\end{array} \qquad (19)
$$

The pressure, p, can be related to the dependent variables by applying the ideal gas law.

$$\mathrm{p} = (\gamma-1)\left[e-\frac{\rho}{2}\mathrm{q}^2\right] \qquad (20)$$

The turbulent viscosity, μ_t, which appears in the viscous matrices, was computed using the Baldwin-Lomax turbulence model.[12]

The thin-layer equations are solved using the PNS technique of Schiff and Steger.[8] Following the approach of Schiff and Steger, the governing equations, which have been modified here to include the Coriolis and centrifugal force terms, are solved using a conservative, approximately factored, implicit finite-difference numerical algorithm as formulated by Beam and Warming.[13]

Following the approach of Schiff and Steger, the equations are first linearized and placed in delta form, where the equations are solved for the difference in the dependent variables rather than the variable itself. This set of equations is then factored using the approach of Beam and Warming. The following set of equations is obtained.

$$\left[\tilde{A}_s^j+(1-\alpha)\Delta\xi\left(\delta_\eta\tilde{B}^j+\tilde{D}^j+\tilde{D}_c^{\,j}\right)\right]\Delta\hat{q}^* = RHS \qquad (21)$$

$$\left[\tilde{A}^j+(1-\alpha)\Delta\xi\left(\delta_\zeta\tilde{C}^j-\frac{1}{Re}\left(\bar{\delta}_\zeta\tilde{M}^j+\tilde{M}_c^{\,j}\right)\right)\right]\Delta\hat{q}^j = \tilde{A}_s^j\Delta\hat{q}^* \qquad (22)$$

$$
\begin{aligned}
RHS &= -(\tilde{A}_s^j-\tilde{A}_s^{j-1})\hat{q}^j+\alpha(\hat{E}_s^j-\hat{E}_s^{j-1})-\left[(\xi_x/J)^{j+1}E_p^j-(\xi_x/J)^jE_p^{j-1}\right] \\
&\quad -(1-\alpha)\Delta\xi\{\delta_\eta\left[\eta_x^{j+1}(E/J)^j+(\eta_\phi/r)^{j+1}(F/J)^j+\eta_r^{j+1}(G/J)^j\right] \\
&\quad +\delta_\zeta\left[\zeta_x^{j+1}(E/J)^j+(\zeta_\phi/r)^{j+1}(F/J)^j+\zeta_r^{j+1}(G/J)^j\right] \\
&\quad +\hat{H}^j+\hat{H}_c^j-\frac{1}{Re}\left(\bar{\delta}_\zeta\tilde{S}^j+\tilde{S}_c^{\,j}\right)+\Phi\} \qquad (23)
\end{aligned}
$$

The form of the equations, as well as the notation, is similar to that used by Schiff and Steger. Here, $\tilde{A}$, $\tilde{B}$, $\tilde{C}$, and $\tilde{M}$ are the Jacobian matrices of the flux vectors $\hat{E}$, $\hat{F}$, $\hat{G}$, and $\hat{S}$.

Further details on the definitions of these matrices can be found in Reference 8. The important difference here is the addition of the matrices $\tilde{D}$ and $\hat{H}$ due to the rotating coordinate system. Although the Jacobian matrix, $\tilde{D}$, can be included in either the circumferential inversion or the normal inversion, including this term in the circumferential inversion simplifies slightly the implementation of the shock fitting boundary conditions. (A listing of the terms in the Jacobian matrix, $\tilde{D}$, is found in the Appendix.) Two additional Jacobian matrices, $\tilde{D}_c$ and $\tilde{M}_c$, appear in these equations and are due to the linearization of the inviscid and viscous cylindrical coordinate source terms, $\hat{H}_c$ and $\hat{S}_c$.

The computations presented here were performed using a shock-fitting procedure reported by Rai and Chaussee.[14] This procedure solves the five Rankine-Hugoniot jump conditions, two geometric shock-propagation conditions, and one compatibility equation to determine the values of the five dependent variables immediately behind the shock, as well as the position of the shock. By including the implicit part of the source term due to the rotating coordinate frame in the circumferential inversion, the shock-fitting procedure of Rai and Chaussee can be used without modification, as long as the correct free-stream conditions are specified as shown here in non-dimensional form.

$$
\begin{aligned}
\rho &= 1 \\
\rho u &= M_\infty \cos\alpha_t + r\Omega_c \sin\alpha_t \cos\phi \\
\rho v &= M_\infty \sin\alpha_t \cos\phi - r\Omega_c \cos\alpha_t + (x - x_{cg})\Omega_c \sin\alpha_t \sin\phi \\
\rho w &= M_\infty \sin\alpha_t \cos\phi - (x - x_{cg})\Omega_c \sin\alpha_t \cos\phi \\
e &= 1./(\gamma(\gamma-1)) + \frac{1}{2}\{M_\infty^2 + r^2\Omega_c^2(\sin^2\alpha_t \cos^2\phi + \cos^2\alpha_t) \\
&\quad -2r(x - x_{cg})\Omega_c^2 \cos\alpha_t \sin\alpha_t \sin\phi + (x - x_{cg})^2\Omega_c^2 \sin^2\alpha_t\}
\end{aligned}
\tag{24}
$$

At the body surface, no-slip, constant wall temperature boundary conditions were applied. For the cases with spin, the circumferential velocity, v, was set equal to the local velocity of the body surface due to solid body rotation.

The computational results presented here were obtained using a grid that consisted of 60 points between the body and the shock. In the circumferential direction, gridding was performed over a 360° sector because of the lack of symmetry from the combination of angle of attack, spin, and coning motion. Thirty-six grid points were used in the circumferential direction. Grid resolution studies showed virtually no difference in the computed aerodynamic coefficients as the number of grid points were increased from 36 to 72 circumferential points using cylindrical coordinates. (Supplementary calculations showed that grid independent solutions required more than 36 points when using Cartesian coordinates.) The computations were performed using a Cray X-MP supercomputer and typically required less than 20 minutes of CPU time for complete calculation over a single configuration.

IV. RESULTS

Computations were performed to determine the aerodynamics of several axisymmetric shell configurations in steady coning motion. The first set of predictions is for two generic

shell configurations: an SOC and an SOCBT. Calculations were performed over a range of Mach numbers and body lengths. The PNS results were compared with Euler code results. A second set of results was obtained for a series of ogive-cylinder configurations (Army-Navy spinner rocket [ANSR]) which were fired through an aerodynamics range located at the former Ballistic Research Laboratory. The computational results are compared with the aerodynamics determined from the in-flight motion of the projectile.

1. Results for the SOC and SOCBT

A schematic of the SOCBT configuration is shown in Figure 4. The SOC is identical to the SOCBT configuration except that the boattail is replaced by a cylinder. The PNS results were compared with pitch-damping results obtained using the inviscid code developed by Schiff.[4] Results were obtained for three body lengths (5, 6, and 7 calibers) and a range of supersonic Mach numbers. The CG position used in the calculations was located at 60% of the body length from the nose. The PNS (viscous) results were obtained using the combined spinning and coning motion approach. The Euler (inviscid) results were obtained using lunar coning motion, since the spin boundary condition required by the combined spinning and coning motion is incompatible with the requirement for zero shear at the body surface in the inviscid approach.

Figures 5 and 6 show the variation of the pitch-damping moment coefficient as a function of Mach number for the three body lengths. In the supersonic regime, the pitch-damping moment shows a decreasing trend with increasing Mach number. The inviscid results at $L/D = 7$ show a maximum near Mach 2. The results also show a significant increase in the pitch-damping moment with increasing body length. The effect of the boattail is to reduce the pitch-damping moment by 20-30% compared with the cylindrical afterbody.

The comparison of the pitch-damping moment predictions from the PNS approach and the Euler approach shows differences of less than 4% across the range of parameters considered here. This is not surprising since the pitch-damping appears to be primarily an inviscid phenomenon. However, the degree of agreement between the PNS and inviscid code is not an absolute indicator of the magnitude of viscous effects since there does appear to be some code-to-code variation of the predicted pitch-damping which is on the order of the viscous effect. The relevance of these differences is probably not significant, especially in light of difficulties in measuring this coefficient experimentally.

The PNS predictions shown previously were obtained using the combined spinning and coning motion. This allowed the pitch-damping force and moment to be determined directly from the side force and moment. As mentioned previously, the accuracy of this approach depends on the degree to which the Magnus moment is accurately predicted. In earlier studies, a numerical capability for determining Magnus force and moment at small angles of attack has been already established.[15] This capability is based on the same numerical approach as applied here.

Figures 7 and 8 show predictions of the Magnus moment coefficient for the cylindrical and boattailed afterbodies. This coefficient would give the expected differences between using lunar coning motion and combined spinning and coning motion to determine the

pitch-damping moment. For the cases examined here, the Magnus moment is less than 4% of the pitch-damping coefficient. The biggest differences were observed for the boattailed configuration, which has a larger Magnus moment and a smaller pitch-damping moment than the SOC configuration. Thus, using lunar coning motion and ignoring the Magnus moment contribution still yields accurate values of the pitch-damping coefficient for the configurations and conditions under consideration here.

The predicted variation of the pitch-damping force coefficient with Mach number for the SOC configuration is shown in Figure 9. These results were obtained from the side force due to combined spinning and coning motion. The results show a strong decrease in the coefficient with increasing Mach number across the range of parameters examined here. The results also show an increase in the coefficient with increasing body length. The PNS results are in good agreement with Euler results.

2. Results for the Army-Navy Spinner Rocket

Computations were performed for the ANSR series of projectiles. These projectiles were fired in an aerodynamics range, and the aerodynamics determined from the projectile motion.[16] The projectiles consisted of a 2-caliber ogive nose with several different length cylindrical bodies, as shown in Figure 10. The total body lengths were 5, 7 and 9 calibers. For each body length, projectiles were fabricated and fired with three different CG locations. This allowed the aerodynamic forces to be determined from the variation of the aerodynamic moments with CG location.

Figures 11 and 12 show the variation of the pitch-damping moment coefficient with CG location for the 5-, 7- and 9-caliber bodies at Mach 1.8 and Mach 2.5, respectively. In both of the figures, the computed results are compared with the experimental measurements. The computational results are considered to be within the accuracy of the experimental measurement and are typically bracketed by the experimental data. For each body length, computations were performed at each of three CG locations. Since the body rotates about the CG, each computation produced a unique flowfield and pitch-damping coefficient. These results are displayed by the triangular symbols in both of these figures. As well, once the aerodynamics of a given configuration are determined, the CG translation relations[1] can be applied to predict the aerodynamic coefficients for the same configuration with a different CG location. Several of these relations are shown below.

$$\begin{aligned}
\hat{C}_{N_\alpha} &= C_{N_\alpha} \\
\hat{C}_{m_\alpha} &= C_{m_\alpha} - s_{cg} C_{N_\alpha} \\
\hat{C}_{N_q} + \hat{C}_{N_{\dot{\alpha}}} &= C_{N_q} + C_{N_{\dot{\alpha}}} + s_{cg} C_{N_\alpha} \\
\hat{C}_{m_q} + \hat{C}_{m_{\dot{\alpha}}} &= C_{m_q} + C_{m_{\dot{\alpha}}} - s_{cg}(C_{N_q} + C_{N_{\dot{\alpha}}}) + s_{cg} C_{m_\alpha} - s_{cg}^2 C_{N_\alpha}
\end{aligned} \tag{25}$$

The aerodynamic coefficients for the modified configuration are denoted by the "^", while the aerodynamic coefficients for the baseline configuration are shown on the right-hand side of the equations. The CG shift, s_{cg}, is in calibers and is positive for a CG shift towards the nose. Using these relations and the predicted aerodynamic coefficients for the middle CG position, the variation of the pitch-damping moment coefficient with CG location was

determined. This variation is shown in Figures 11 and 12 by the solid line. The difference between the pitch-damping moment coefficients predicted from the CG translation relations and the pitch-damping moment as determined from the direct computations is less than 0.1% . This serves as a consistency check for the computational approach.

It is noted that at both Mach numbers, for the middle CG position of the 9-caliber body, there are several experimental data points which deviate from the trend shown by the predictions and the apparent trend shown by the experimental data. The cause of this deviation is unknown.

As seen above from the CG translation relations, the pitching moment coefficient varies linearly with the CG shift. The slope of the variation is the normal force coefficient slope, C_{N_α}. By firing projectiles with the same external shape but with different CG positions, the normal force can thus be determined from the variation of the pitching moment with CG location. A similar approach can be used to determine the pitch-damping force coefficient from the variation of the pitch-damping moment coefficient with CG location. Because the pitch-damping moment varies in a nonlinear fashion with the CG shift, a modified damping moment is defined as

$$\hat{C}_{m_q} + \hat{C}_{m_{\dot{\alpha}}} - s_{cg}\hat{C}_{m_\alpha} = C_{m_q} + C_{m_{\dot{\alpha}}} - s_{cg}(C_{N_q} + C_{N_{\dot{\alpha}}}) \quad . \tag{26}$$

When the left hand side of this equation is plotted as a function of CG shift, the results should be a line with slope equal to the pitch-damping force coefficient. For all practical purposes, the determination of the pitch-damping force from range firings can only be obtained from the variation of the pitch-damping moment with CG locations because the pitch-damping force coefficient contributes little to the in-flight motion of the projectile. Hence, direct determination is not practical.

From the CG variation of the pitch-damping moment, the pitch-damping force coefficient was determined from the experimental measurements. Figure 13 shows the variation of the pitch-damping force coefficient with body length for the middle center of gravity location. Note that, unlike the normal force coefficient, the pitch-damping force varies with CG position. The agreement between the computational predictions and experimental results are within the experimental accuracy and show the correct variation with body length and Mach number.

As mentioned previously, the pitch-damping predictions were obtained using the combined spinning and coning motion which allows the pitch-damping force and moment to be determined directly from the side force and moment. The expected differences between applying combined spinning and coning motions, and lunar coning motion are reflected in the Magnus moment coefficient. In the current effort, the Magnus force and moment have been computed for the ANSR configuration and comparison made with range data obtained from the same series of firings as shown in Figures 14 and 15. The computed results were obtained for a fully turbulent boundary layer, although there is some evidence from the experimental program to indicate laminar flow over a portion of the body, particularly near the nose. The computational results are within the scatter of the experimental data for most of the CG positions although several of the cases show an overprediction by as much as 30-40%. The predictions show that determining the pitch-damping coefficient directly from the side moment due to lunar coning motion (which requires the Magnus moment to be ignored) will

result in errors of less than 5% for this configuration.

Finally, using the Magnus results discussed here and the side force and moment due to lunar coning motion, predictions of the pitch-damping coefficients (Equations 7 and 9) were made and compared with the predictions of the pitch-damping coefficients obtained using a single calculation utilizing combined spinning and coning motion. The maximum difference between the two approaches was less that 0.1% . This demonstrates the lack of coupling between the spinning and coning motions over the range of coning rates, spin rates, and angles of attack considered here. (It is interesting to note that at higher angles of attack, a nonlinear variation of Magnus moment with angle of attack was predicted. Even at these angles of attack, no coupling between the coning and spinning motions was observed.)

V. CONCLUSION

A computational approach for predicting the pitch-damping coefficients using steady coning motion has been successfully applied to several axisymmetric shell configurations. Through the use of a combined spinning and coning motion, the pitch-damping force and moment have been obtained directly from the side force and moment using a single calculation. This approach does not require that the Magnus force or moment be ignored or determined from an auxiliary calculation, as in the case of lunar coning motion.

The computational predictions for the SOC and SOCBT configurations showed good agreement with results obtained with a previously published inviscid code. The results showed an increasing trend in the pitch-damping coefficient with increasing length-to-diameter ratio and a decreasing trend in the coefficient with increasing Mach number. The presence of the boattail on the projectile produced a significant reduction in the pitch-damping moment compared with an equivalent length cylindrical afterbody. The predictions of both the pitch-damping force and moment coefficients for the ANSR were seen to be in excellent agreement with the data obtained from aerodynamic range testing. The computational results predicted the correct variation in the pitch-damping moment coefficient with changing center of gravity location, body length, and Mach number. For each of the configurations examined here, the effect of viscosity on the pitch-damping coefficients was small.

The use of the combined spinning and coning motion is currently being applied to time marching codes for the prediction of pitch-damping at subsonic through low supersonic velocities. In this velocity regime, it is expected that viscous effects will be of greater importance than in the supersonic regime examined here.

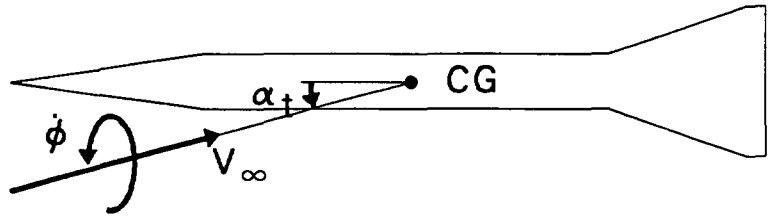

Figure 1. Schematic of coning motion.

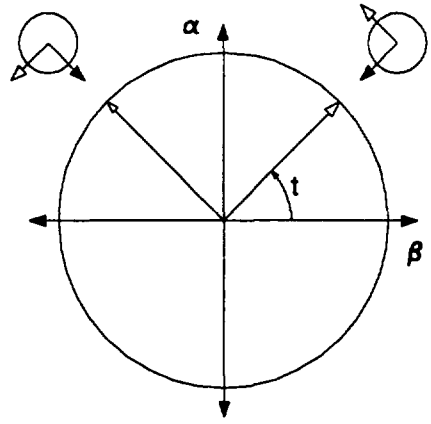

Figure 2. Coning motion with respect to non-rolling coordinates.

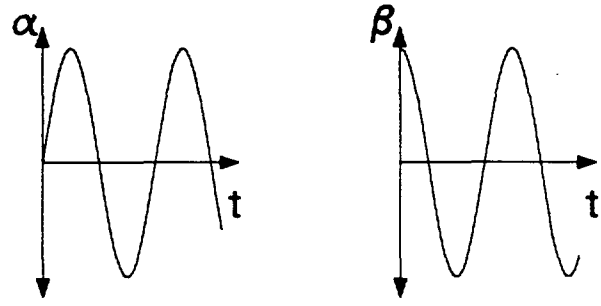

Figure 3. Components of coning motion.

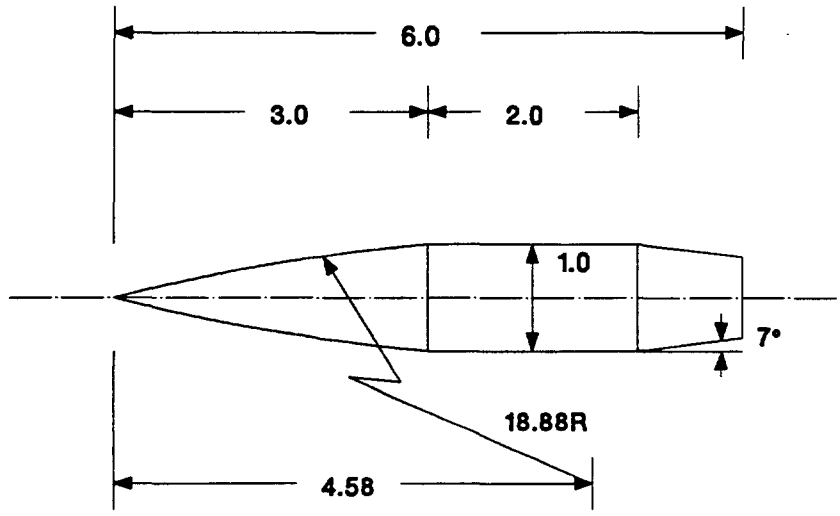

Figure 4. Schematic of the SOCBT configuration.

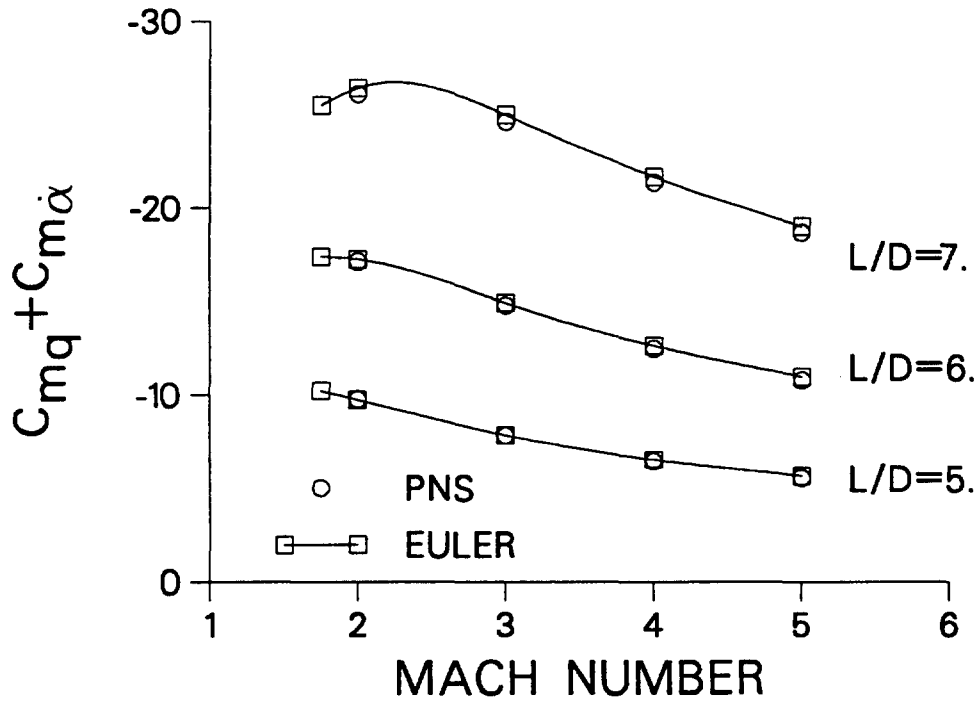

Figure 5. Pitch-damping moment coefficient versus Mach number for various body lengths, SOC configuration.

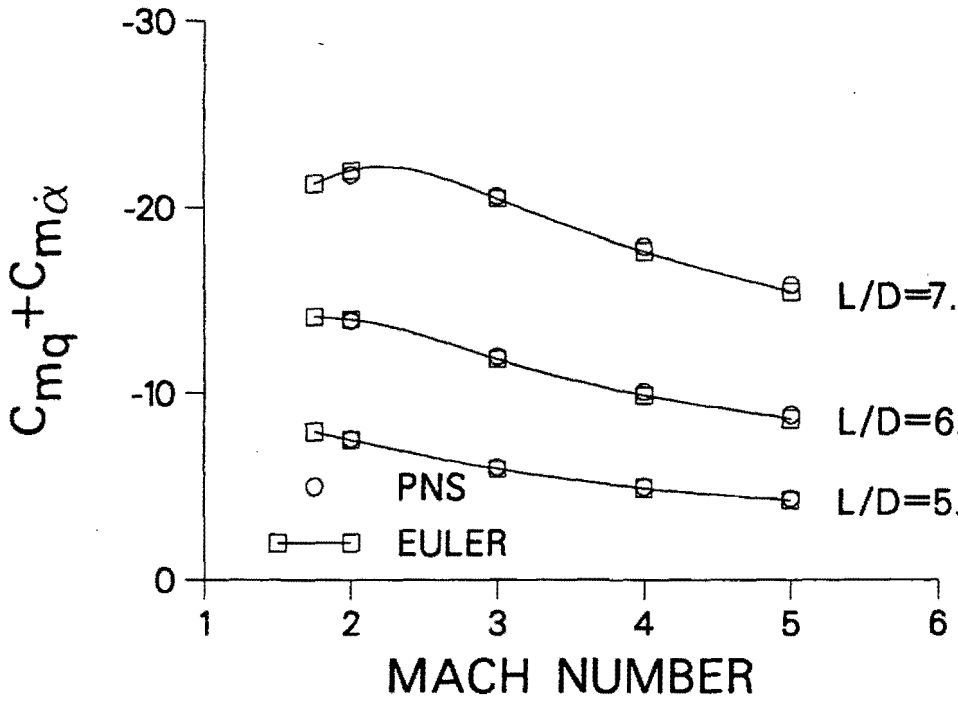

Figure 6. Pitch-damping moment coefficient versus Mach number for various body lengths, SOCBT configuration.

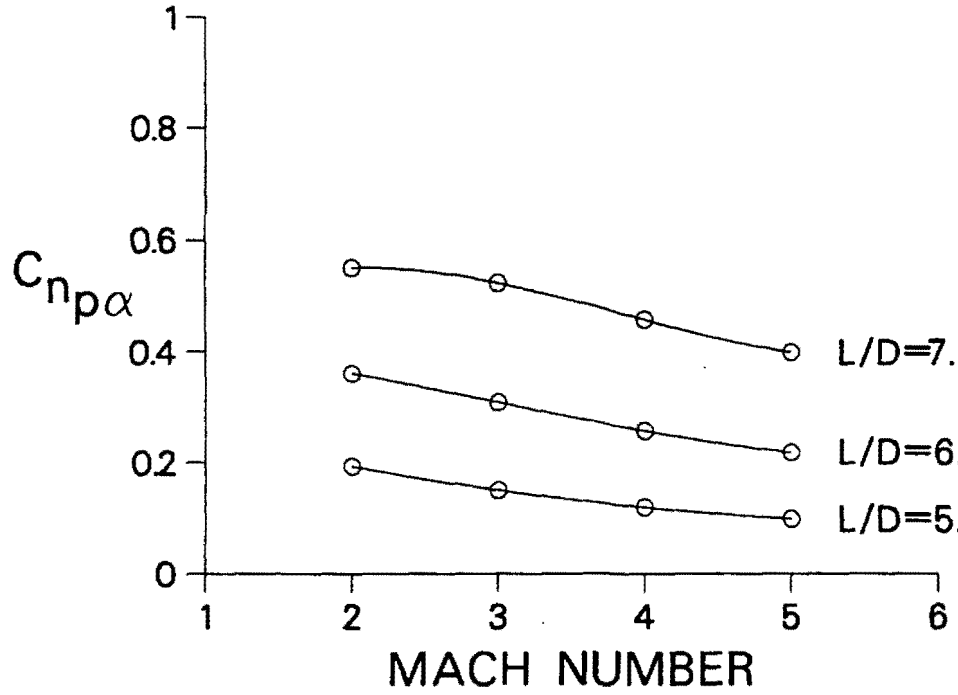

Figure 7. Magnus moment coefficient versus Mach number for various body lengths, SOC configuration.

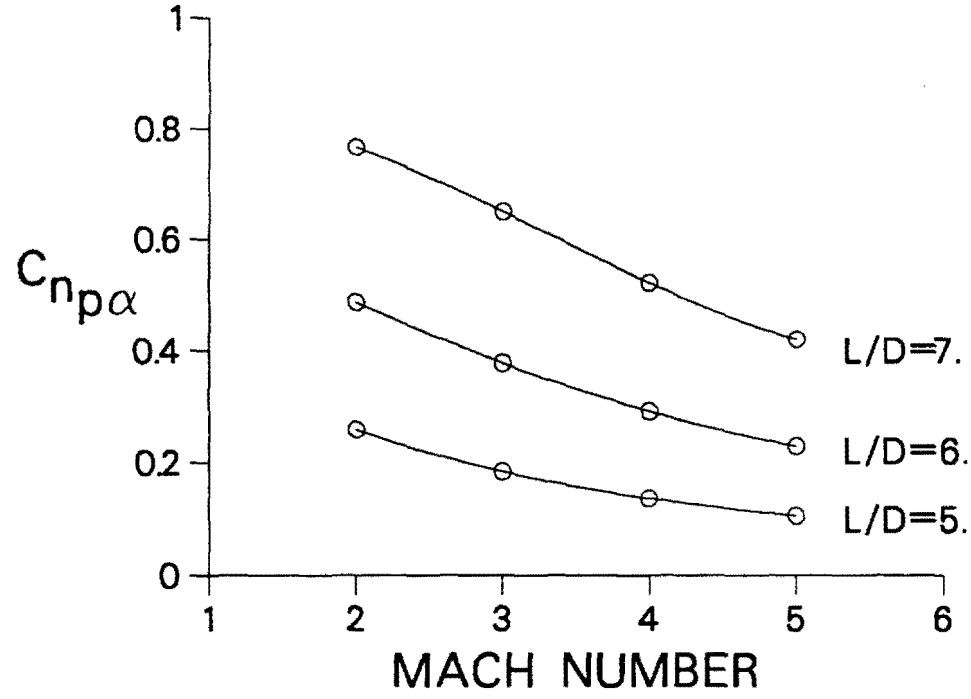

Figure 8. Magnus moment coefficient versus Mach number for various body lengths, SOCBT configuration.

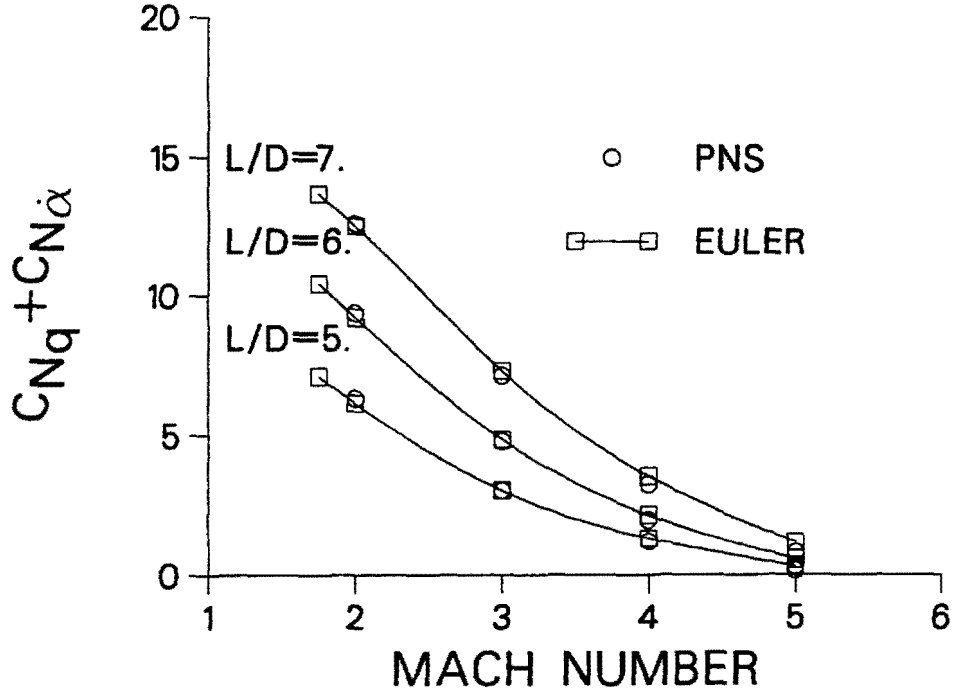

Figure 9. Pitch-damping force coefficient versus Mach number for various body lengths, SOC configuration.

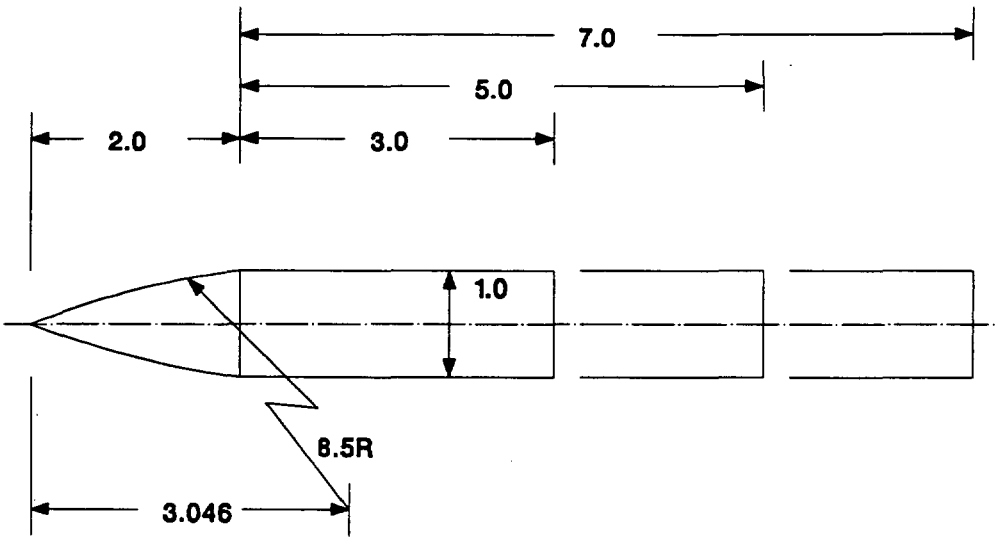

Figure 10. Schematic of the ANSR.

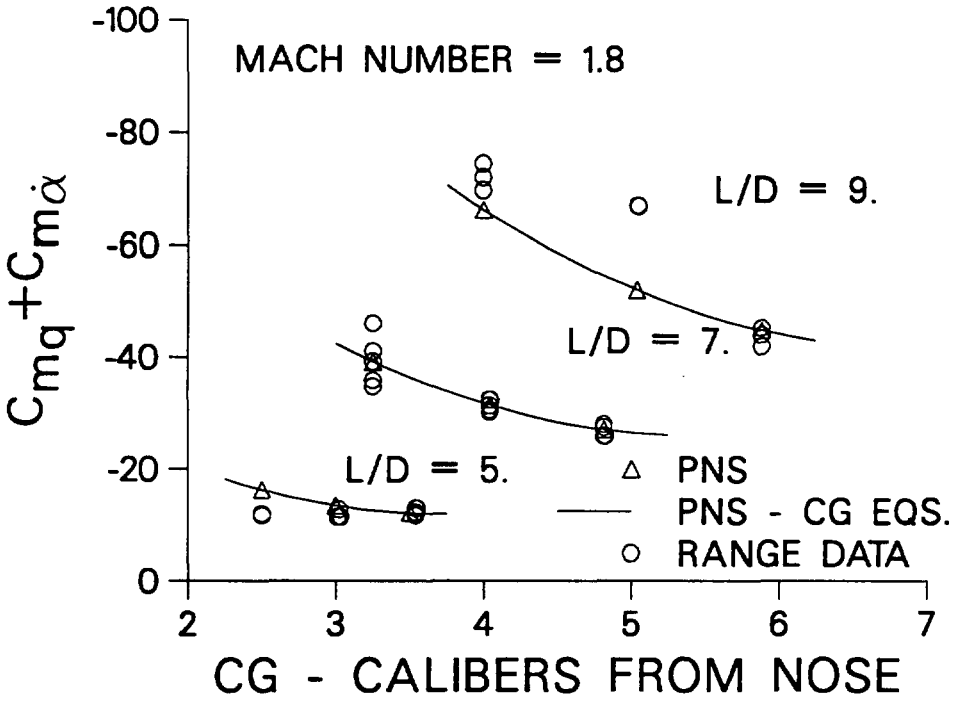

Figure 11. Pitch-damping moment coefficient versus CG location, Mach 1.8, ANSR.

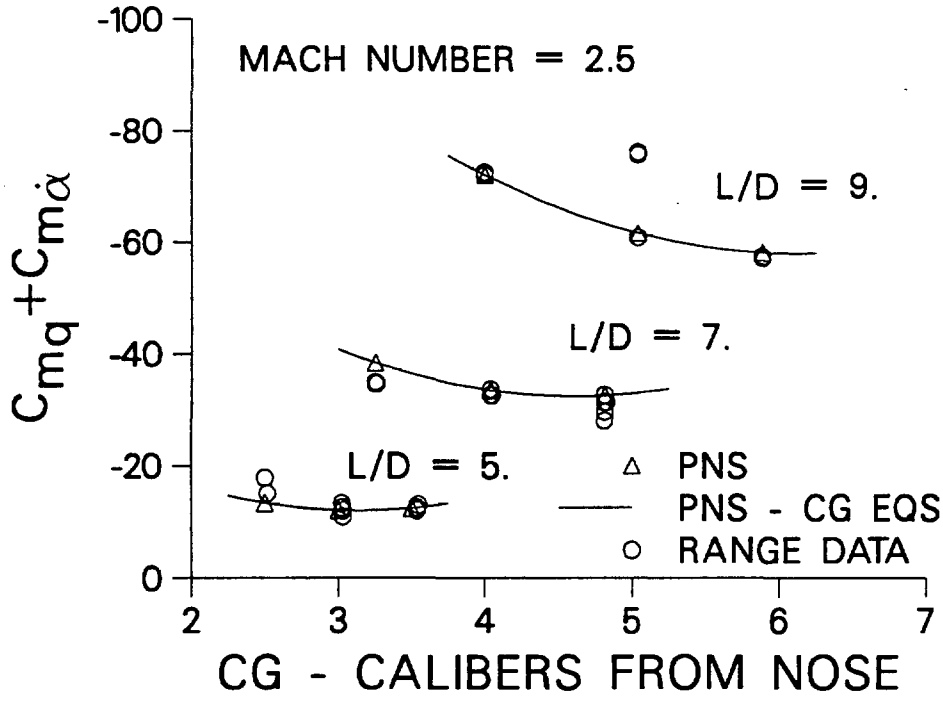

Figure 12. Pitch-damping moment coefficient versus CG location, Mach 2.5, ANSR.

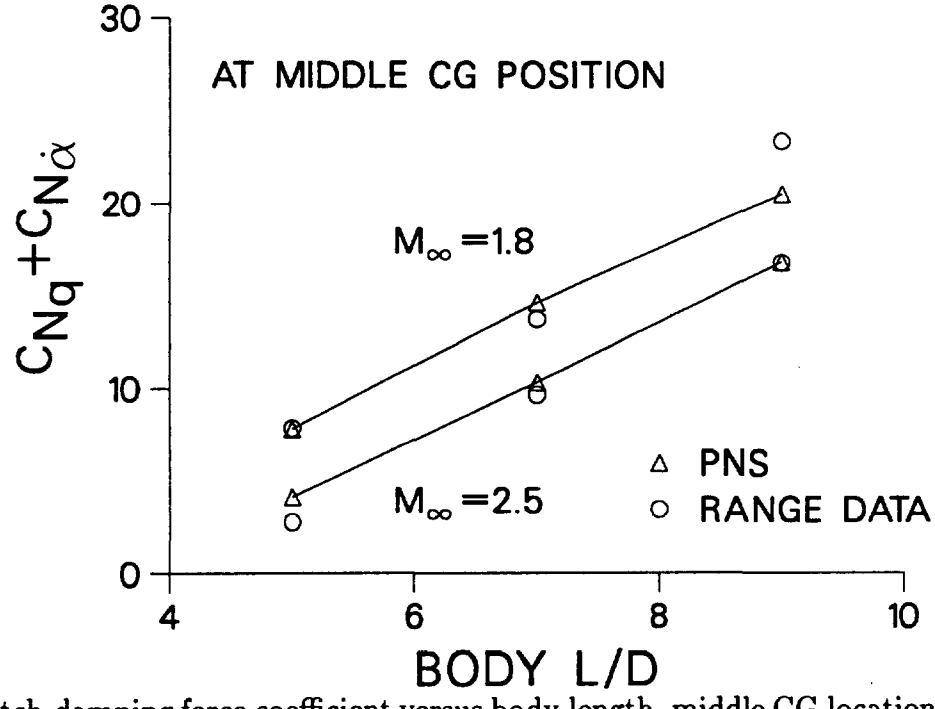

Figure 13. Pitch-damping force coefficient versus body length, middle CG location , ANSR.

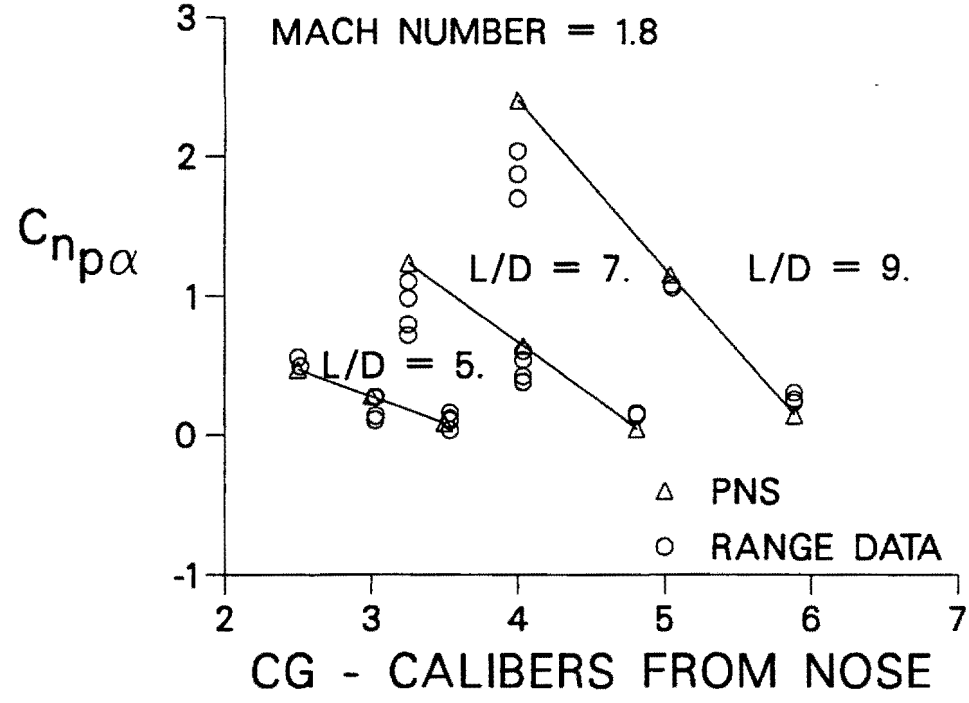

Figure 14. Magnus moment coefficient versus CG location, Mach 1.8, ANSR.

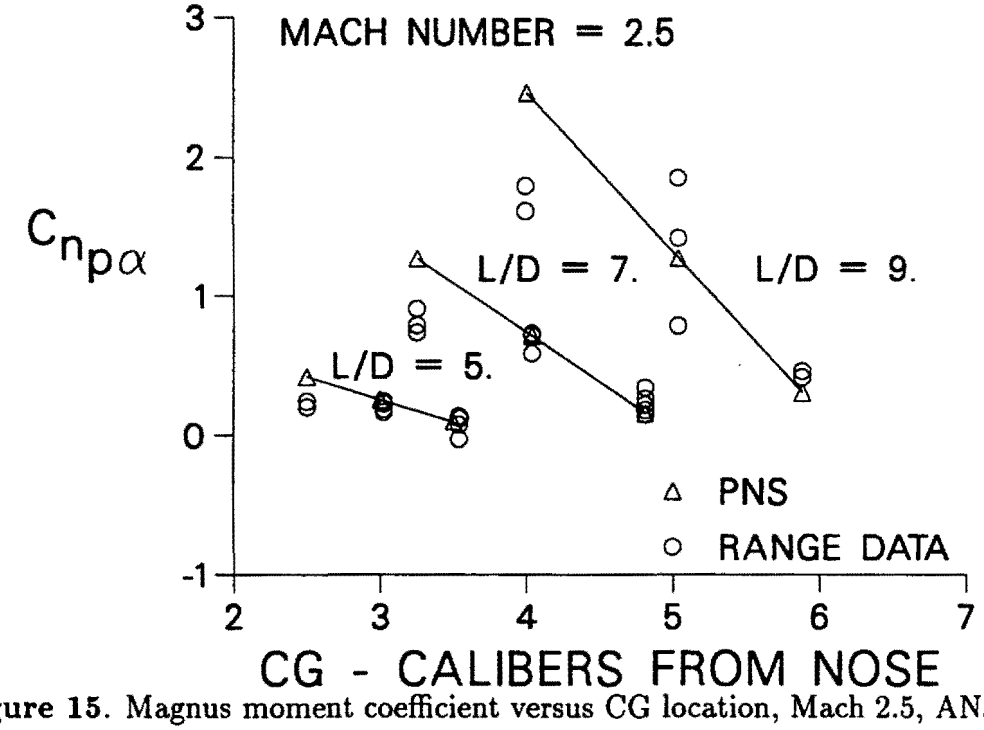

Figure 15. Magnus moment coefficient versus CG location, Mach 2.5, ANSR.

INTENTIONALLY LEFT BLANK.

References

1. Murphy, C.H., "Free Flight Motion of Symmetric Missiles," U.S. Army Ballistic Research Laboratory, Aberdeen Proving Ground, Maryland, Report No. 1216, July 1963. (AD A442757)

2. Tobak, M., Schiff, L.B., and Peterson, V.L., "Aerodynamics of Bodies of Revolution in Coning Motion," AIAA Journal, Vol. 7, No. 1, January 1969, pp. 95-99.

3. Schiff, L.B., and Tobak, M., "Results from a New Wind-Tunnel Apparatus for Studying Coning and Spinning Motions of Bodies of Revolution", AIAA Journal, Vol. 8, No. 11, November 1970, pp. 1953-1957.

4. Schiff, L.B., "Nonlinear Aerodynamics of Bodies in Coning Motion", AIAA Journal, Vol. 10, No. 11, November 1972, pp. 1517-1522.

5. Agarwal, R., and Rakich, J.V., "Computation of Supersonic Laminar Viscous Flow Past a Pointed Cone at Angle of Attack in Spinning and Coning Motion", AIAA Paper 78-1211, AIAA 11th Fluid and Plasma Dynamics Conference, July 1978.

6. Lin, T.C., "A Numerical Study of the Aerodynamics of a Reentry Vehicle in Steady Coning Motion", AIAA Paper 78-1358, AIAA Atmospheric Flight Mechanics Conference, Palo Alto, CA, August 1978.

7. Weinacht, P., and Sturek, W.B., "Navier-Stokes Predictions of Pitch Damping for Finned Projectiles Using Steady Coning Motion," AIAA Paper 90-3088, AIAA 8th Applied Aerodynamics Conference, August 1990.

8. Schiff, L.B., and Steger, J.L., "Numerical Simulation of Steady Supersonic Viscous Flow," AIAA Journal, Vol. 18, No. 12, December 1980, pp. 1421-1430.

9. Levy, L.L., and Tobak, M., "Nonlinear Aerodynamics of Bodies of Revolution in Free Flight", AIAA Journal, Vol. 8, No. 12, December 1970, pp. 2168-2171.

10. Tobak, M., and Schiff, L.B., "Generalized Formulation of Nonlinear Pitch-Yaw-Roll Coupling: Part I - Nonaxisymmetric Bodies," AIAA Journal, Vol. 13, No. 3, March 1975, pp. 323-326.

11. Tobak, M., and Schiff, L.B., "Generalized Formulation of Nonlinear Pitch-Yaw-Roll Coupling: Part II - Nonlinear Coning Rate," AIAA Journal, Vol. 13, No. 3, March 1975, pp. 327-332.

12. Baldwin, B.S., and Lomax, H., "Thin Layer Approximation and Algebraic Model for Separated Turbulent Flows," AIAA Paper 78-257, 16th Aerospace Sciences Meeting, January 1978.

13. Beam, R., and Warming, R.F., "An Implicit Factored Scheme for the Compressible Navier-Stokes Equations," AIAA Journal, Vol. 16, No. 4, 1978, pp. 85-129.

14. Rai, M.M., and Chaussee, D.S., "New Implicit Boundary Procedure: Theory and Applications," AIAA Paper 83-0123, January 1983.

15. Sturek, W.B., and Schiff, L.B., "Computations of the Magnus Effect for Slender Bodies in Supersonic Flight," U.S. Army Ballistic Research Laboratory, Aberdeen Proving Ground, Maryland, Technical Report No. 2384, December 1981, ADA110016. (Also see, Sturek, W.B., and Schiff, L.B., "Computations of the Magnus Effect for Slender Bodies in Supersonic Flight," AIAA Paper 80-1586-CP, AIAA Atmospheric Flight Mechanics Conference, August 1980.

16. Murphy, C.H., and Schmidt, L.E., "The Effect of Length on the Aerodynamics Characteristics of Bodies of Revolution in Supersonic Flight," U.S. Army Ballistic Research Laboratory, Aberdeen Proving Ground, Maryland, Report No. 876, August 1953, AD023468.

LIST OF SYMBOLS

a	speed of sound
C_m	pitching moment coefficient
C_{m_α}	slope of the pitching moment coefficient with angle of attack
$C_{m_q} + C_{m_{\dot{\alpha}}}$	pitch-damping moment coefficient
C_n	side moment coefficient
$C_{n_{\dot{\phi}}}$	slope of the side moment coefficient with coning rate
$C_{n_{p\alpha}}$	Magnus moment coefficient
C_{N_α}	slope of the normal force coefficient with angle of attack
$C_{N_q} + C_{N_{\dot{\alpha}}}$	pitch-damping force coefficient
D	projectile diameter
e	total energy per unit volume, non-dimensionalized by $\rho_\infty a_\infty^2$
$\hat{E}, \hat{F}, \hat{G}$	flux vectors in transformed coordinates
$\hat{H}$	source term resulting from rotating coordinate frame
J	Jacobian
l	characteristic length, typically the projectile diameter
L	projectile body length
M_∞	free-stream Mach number
p	pressure, as used in thin-layer Navier-Stokes equations, non-dimensionalized by $\rho_\infty a_\infty^2$
p	spin rate in non-rolling coordinate frame, as used in the aerodynamic moment equations and coefficients
p_{cf}	spin rate in coning reference frame
Pr	Prandtl number
Pr_t	turbulent Prandtl number
Re	Reynolds number, $a_\infty \rho_\infty D/\mu_\infty$
r	radial coordinate, non-dimensionalized by D
s	distance downrange
s_{cg}	center of gravity shift, calibers
$\hat{S}$	viscous flux vector in transformed coordinates
t	time
u, v, w	velocity components in x, y, and z directions, non-dimensionalized by a_∞
U, V, W	Contravariant velocities of the transformed Navier-Stokes equations
V	free-stream velocity used to non-dimensionalize the coning rate, spin rate, and the aerodynamic coefficients
x, y, z	axial, horizontal, and vertical coordinates with respect to the body
x_{cg}	axial location of projectile center of gravity with respect to the axial coordinate, x

Greek Symbols

α	vertical component of angle of attack in non-rolling coordinates

α_t	total angle of attack, $\sqrt{\alpha^2 + \beta^2}$
β	horizontal component of angle of attack in non-rolling coordinates
γ	ratio of specific heats, as used in Navier-Stokes equations
γ	cosine of the total angle of attack, as used in aerodynamic force and moment formulations
δ	sine of the total angle of attack
μ	laminar viscosity
μ_t	effective turbulent eddy viscosity
ξ, η, ζ	transformed coordinates in Navier-Stokes equations
$\tilde{\xi}$	complex quantity representing the components of the sine of the angle of attack with respect to the non-rolling coordinate frame
ρ	density, normalized by ρ_∞
ϕ	circumferential coordinate as measured from vertical axis
$\dot{\phi}$	coning rate of projectile
$\frac{\dot{\phi}D}{V}$	nondimensional coning rate
Ω_c	coning rate of projectile, non-dimensionalized by a_∞/D

Superscripts

$\dot{(\ )}$	rate of change with respect to time
$(\ )'$	rate of change with respect to space
$\tilde{(\ )}$	quantity is referenced to the non-rolling coordinate frame

Subscripts

(∞)	denotes quantity evaluated at free-stream condition

APPENDIX

This appendix provides a listing of the terms in the Jacobian matrix, $\tilde{D}^j$, of the source term, $\hat{H}$. The superscript, j, denotes that $\tilde{D}$ is to be evaluated at axial station j. The components of the Jacobian matrix, $\tilde{D}$ are determined from the source term, $\hat{H}$, as follows.

$$D_{mn} = \frac{\partial H_m}{\partial q_n} \tag{27}$$

The non-zero elements of the Jacobian matrix are shown below.

$$\begin{aligned}
D_{21} &= r\Omega_c^2 \sin\alpha_t \cos\alpha_t \cos\phi - (x - x_{cg})\Omega_c^2 \sin^2\alpha_t \\
D_{23} &= 2\Omega_c \sin\alpha_t \cos\phi \\
D_{24} &= -2\Omega_c \sin\alpha_t \sin\phi \\
D_{31} &= (x - x_{cg})\Omega_c^2 \sin\alpha_t \cos\alpha_t \sin\phi + r\Omega_c^2 \sin^2\alpha_t \cos\phi \sin\phi \\
D_{32} &= -2\Omega_c \sin\alpha_t \cos\phi \\
D_{34} &= 2\Omega_c \cos\alpha_t \\
D_{41} &= -r\Omega_c^2 \sin^2\alpha_t \sin\phi - r\Omega_c^2 \cos^2\alpha_t + (x - x_{cg})\Omega_c^2 \sin\alpha_t \cos\alpha_t \cos\phi \\
D_{42} &= 2\Omega_c \sin\alpha_t \sin\phi \\
D_{43} &= -2\Omega_c \cos\alpha_t \\
D_{52} &= -(x - x_{cg})\Omega_c^2 \sin^2\alpha_t \cos^2\alpha_t + r\Omega_c^2 \sin\alpha_t \cos\alpha_t \cos\phi \\
D_{53} &= (x - x_{cg})\Omega_c^2 \cos\alpha_t \sin\alpha_t \sin\phi + r\Omega_c^2 \sin^2\alpha_t \cos\phi \sin\phi \\
D_{54} &= (x - x_{cg})\Omega_c^2 \sin\alpha_t \cos\alpha_t \cos\phi - r\Omega_c^2 \sin^2\alpha_t \sin^2\phi - r\Omega_c^2 \cos^2\alpha_t
\end{aligned}$$

INTENTIONALLY LEFT BLANK.

No. of Copies	Organization
2	Administrator Defense Technical Info Center ATTN: DTIC-DDA Cameron Station Alexandria, VA 22304-6145
1	Commander U.S. Army Materiel Command ATTN: AMCAM 5001 Eisenhower Ave. Alexandria, VA 22333-0001
1	Director U.S. Army Research Laboratory ATTN: AMSRL-OP-SD-TA, Records Management 2800 Powder Mill Rd. Adelphi, MD 20783-1145
3	Director U.S. Army Research Laboratory ATTN: AMSRL-OP-SD-TL, Technical Library 2800 Powder Mill Rd. Adelphi, MD 20783-1145
1	Director U.S. Army Research Laboratory ATTN: AMSRL-OP-SD-TP, Technical Publishing Branch 2800 Powder Mill Rd. Adelphi, MD 20783-1145
2	Commander U.S. Army Armament Research, Development, and Engineering Center ATTN: SMCAR-TDC Picatinny Arsenal, NJ 07806-5000
1	Director Benet Weapons Laboratory U.S. Army Armament Research, Development, and Engineering Center ATTN: SMCAR-CCB-TL Watervliet, NY 12189-4050
1	Director U.S. Army Advanced Systems Research and Analysis Office (ATCOM) ATTN: AMSAT-R-NR, M/S 219-1 Ames Research Center Moffett Field, CA 94035-1000

No. of Copies	Organization
1	Commander U.S. Army Missile Command ATTN: AMSMI-RD-CS-R (DOC) Redstone Arsenal, AL 35898-5010
1	Commander U.S. Army Tank-Automotive Command ATTN: AMSTA-JSK (Armor Eng. Br.) Warren, MI 48397-5000
1	Director U.S. Army TRADOC Analysis Command ATTN: ATRC-WSR White Sands Missile Range, NM 88002-5502
1	Commandant U.S. Army Infantry School ATTN: ATSH-WCB-O Fort Benning, GA 31905-5000
	Aberdeen Proving Ground
2	Dir, USAMSAA ATTN: AMXSY-D AMXSY-MP, H. Cohen
1	Cdr, USATECOM ATTN: AMSTE-TC
1	Dir, USAERDEC ATTN: SCBRD-RT
1	Cdr, USACBDCOM ATTN: AMSCB-CII
1	Dir, USARL ATTN: AMSRL-SL-I
5	Dir, USARL ATTN: AMSRL-OP-AP-L

DISTRIBUTION LIST

No. Copies	Organization
AH43:	
1	HQDA (SARD-TR/Ms. K. Kominos) Washington, DC 20310-0103
1	HQDA (SARD-TR/Dr. R. Chait) Washington, DC 20310-0103
2	Honeywell, INC. ATTN: Mark W. Swenson Richard J. Buretta Mail Station MN11-2626 600 Second Street, North East Hopkins, MN 55343
1	Arrow Technology Associates ATTN: Robert Whyte P.O. Box 4218 Burlington, VT 05491-0042
2	WL/FIMC Air Force Materiel Command ATTN: Joe Manter Don Kinsey 2645 Fifth St., Ste. 7 Wright-Patterson AFB, OH 45433-7913
3	Martin Marietta Astro Space ATTN: Dr. James E. Daywitt Dr. David Szostowski Dr. Robert Brewer Mail Stop U-4019 Mall Blvd King of Prussia, PA 19406
2	Commander Naval Surface Warfare Center Applied Mathematics Branch ATTN: Code R44 (Mr. F. Priolo) Code R44 (Dr. A. Wardlaw) White Oak Laboratory Silver Spring, MD 20903-5000
1	Director Sandia National Laboratories ATTN: Dr. W. Oberkampf Division 1636 Albuquerque, NM 87185
9	Commander Armament R&D Center US Army AMCCOM SMCAR-LCA-F ATTN: C. Ng M. Amoruso S. Kahn J. Grau H. Hudgins W. Toledo C. Livecchia B. Wong S. Chung Picatinny Arsenal, NJ 07806-5000
3	Director National Aeronautics and Space Administration Ames Research Center ATTN: M/S N227-8, L. Schiff M/S N258-1, D. Chaussee M/S N258-1, G. Molvik Moffett Field, CA 94035
4	Director Air Force Armament Laboratory Aeromechanics Division Aerodynamics Branch ATTN: Mr. Gregg Abate Capt. Roger S. Gates Mr. Gerald L. Winchenbach Mr. John R. Cipolla Eglin AFB, FL 32542-5000
1	Director Air Force Armament Laboratory AFATL/FXA ATTN: Dr. Dave Belk Eglin AFB, FL 32542-5000
2	VRA Inc. ATTN: Dr. C. Lewis Dr. B.A. Bhutta P.O. Box 50 Blacksburg, VA 24060

DISTRIBUTION LIST

No. Copies	Organization
1	Commander U.S. Army Missile Command ATTN: AMSMI-RD-SS-AT B. Walker Redstone Arsenal, AL 35898-5010
1	Science Applications, Inc. Computational Fluid Dynamics Division ATTN: Dr. D. W. Hall 994 Old Eagle School Road Suite 1018 Wayne, PA 19087
1	McDonnell Douglas Missile Systems Co. ATTN: F. McCotter Mailcode 306-4249 P.O. Box 516 St. Louis, MO 63166-5016
1	University of Maryland Department of Aerospace Engineering ATTN: Dr. J.D. Anderson, Jr. College Park, MD 20742
1	University of Texas Department of Aerospace Engineering and Engineering Mechanics ATTN: Dr. D.S. Dolling Austin, TX 78712-1055
3	Institute for Advanced Technology ATTN: Dr. W.G. Reineke Dr. T. Kiehne Dr. D. Barnette 4030-2 W. Braker Lane Austin, TX 78759-5329
3	Commander Armament R&D Center US Army AMCCOM ATTN: AMCPM-TMA (Col. Mullen) AMCPM-TMA-105 (C. Kimker) AMCPM-TMA-120 (C. Roller) Picatinny Arsenal, NJ 07806-5000
1	Commander U.S. Army Armament R, D & E Center ATTN: SMCAR-FSF-T (Mr. B. McCoy) Aberdeen Proving Ground, MD 21005-5001
1	Commander Armament R&D Center US Army AMCCOM SMCAR-CCH-V ATTN: Ed Fennell Picatinny Arsenal, NJ 07806-5000
1	Commander US Naval Surface Weapons Center ATTN: Dr. F. Moore Dahlgren, VA 22448
1	US Army Research Office ATTN: T. Doligowski P.O. Box 12211 Research Triangle Park, NC 27709-2211
2	Kaman Sciences Corp. ATTN: R. Prozan T. Hayden 1500 Garden of the Gods Rd. Colorado Springs, CO 80907
	Aberdeen Proving Ground
14	Director, USARL ATTN: AMSRL-WT-W, Dr. C. Murphy AMSRL-WT-WB, Dr. W. D'Amico AMSRL-CI-C, Dr. W. Sturek AMSRL-WT-P, Mr. A. Horst AMSRL-WT-PB, Dr. E. Schmidt AMSRL-WT-PB, Dr. P. Plostins AMSRL-WT-PB, Mr. V. Oskay AMSRL-WT-PB, Mr. C. Nietubicz AMSRL-WT-PB, Dr. J. Sahu AMSRL-WT-PB, Mr. P. Weinacht AMSRL-WT-PB, Mr. H. Edge AMSRL-WT-PB, Mr. B. Guidos AMSRL-WT-PB, Mr. E. Ferry AMSRL-WT-PB, Ms. K. Heavey

INTENTIONALLY LEFT BLANK.